Journal of Power Sources 196 (2011) 98–109

Contents lists available at ScienceDirect

Journal of Power Sources

journal homepage: www.elsevier.com/locate/jpowsour

Mesoscale-structure control at anode/electrolyte interface in solid oxide fuel cell

Akio Konno[a,*], Hiroshi Iwai[a], Kenji Inuyama[a], Atsushi Kuroyanagi[a], Motohiro Saito[a], Hideo Yoshida[a], Kazufumi Kodani[b], Kuniaki Yoshikata[b]

[a] Department of Aeronautics and Astronautics, Kyoto University, Yoshida Honmachi, Sakyo-ku, Kyoto 606-8501, Japan
[b] Dai Nippon Printing Co., Ltd., Japan

ARTICLE INFO

Article history:
Received 7 April 2010
Received in revised form 30 June 2010
Accepted 8 July 2010
Available online 15 July 2010

Keywords:
Solid oxide fuel cell
Mesoscale structure
Interface area enlargement
Single-cell experiment
Numerical simulation

ABSTRACT

To enhance the power density of a solid oxide fuel cell, a mesoscale-structure control of an electrode/electrolyte interface was proposed; here, the mesoscale means a size range of 10–100 μm, which is larger than the microscale of the electrode particles but smaller than the macroscale of the cell geometries. Therefore, the mesoscale structure does not only change the local thickness of the electrolyte and electrode but also enlarge the electrode/electrolyte interface area, and thus influence the cell performance. First, to find effective conditions for the mesoscale-structure control, a preliminary theoretical analysis in a conventional flat cell was performed focusing on the ratio of the ion-conducting resistance to the reaction resistance. In the light of this basic knowledge, as a second step, the effects of the mesoscale structure on an anode side of an electrolyte-supported cell were studied numerically and experimentally. A 2D numerical simulation based on an equivalent electrical circuit model and the dusty-gas model was carried out. As a result, the mesoscale-grooved structure was found to be effective for enhancement of the power generation, if the groove scale is sufficiently larger than that of the active reaction region of the electrode. Qualitatively similar results were obtained from the experiments using a segmented electrode with both flat and mesoscale-grooved surface in a button-type cell.

1. Introduction

Solid oxide fuel cells (SOFCs) directly convert the chemical energy of gases into electrical energy and are used as high-efficiency power generation devices. Numerous basic studies on SOFCs for the development of cell materials [1,2] and the investigation of cell design [3–9] have been performed. On the other hand, many researchers have recently focused on improving the durability and reducing the cost of SOFC systems for practical implementation [10–14]. Increasing the power density of SOFCs enables their size and weight to be reduced. This reduction is one of the important ways of reducing the material cost and enhancing the load-following capability owing to the decreased heat capacity of the cells.

Various methods of increasing the power density of a cell have been proposed and investigated. From the viewpoint of the geometric characteristic length, the proposed methods can be classified into three types based on the characteristic length. The first is the modification of the cell design, which corresponds to a macroscopic-structure approach (≥1 mm). There are three general types of cell design: tubular, flat, and flat-tube types, and attempts have been made to optimize each type of cell design [5–9]. The second is a microstructure change (0.1–1 μm), which is related to the properties of the porous electrode microstructure, such as the porosity, volume fraction, the tortuosity of the gas phase and electrical-conducting phase, and the density of the electrochemical reaction site called the three-phase boundary (TPB), where the electrons, oxygen ions, and reactant gas meet. A multilayer electrode [15–17] is often used to locally increase the TPB density, because it is considered that the electrochemical reaction actively takes place at the TPB near the electrode/electrolyte interface, although the TPB exists throughout a composite electrode [18,19]. An increase in the power density is achieved by applying a multilayer with a fine microstructure near the electrolyte. Such an approach based on a microstructure change is highly effective, because it can be applied to a structure with a wide range of geometric characteristic lengths. However, degradation of the microstructure has been observed in long-term operation [11–13].

The third approach to increasing the power density of a cell is modification at a scale between those of the above methods, referred to as a mesoscale-structure change (10–100 μm). Such a change is at a scale smaller than the macroscopic-structure change of a cell and larger than the microstructure change of the porous electrodes. For instance, mesoscale-structure changes involve micron-scale thickness control of the electrodes and electrolyte [20] and micron-scale control of the electrode/electrolyte

* Corresponding author. Tel.: +81 75 753 5203; fax: +81 75 753 5203.
E-mail address: konno@t06.mbox.media.kyoto-u.ac.jp (A. Konno).

0378-7753/$ – see front matter © 2010 Elsevier B.V. All rights reserved.
doi:10.1016/j.jpowsour.2010.07.025

Nomenclature

ASR	area-specific resistance ($\Omega\,m^2$)
Bi	Biot number
Bi_{FC}	fuel cell Biot number
D_{ij}	binary diffusivity ($m^2\,s^{-1}$)
$D_{i,K}$	Knudsen diffusivity of chemical component i ($m^2\,s^{-1}$)
d	diameter (m)
E_0	*EMF* at standard state (V)
F	Faraday constant ($C\,mol^{-1}$)
I	current (A)
i	current density ($A\,m^{-2}$)
i_0	exchange current density ($A\,m^{-2}$)
i^L_{tpb}	current per unit TPB length ($A\,m^{-1}$)
i_{ct}	volume-specific charge transfer current ($A\,m^{-3}$)
K	permeability (m^2)
k_K	Kozeny constant
l	thickness or height (m)
l_{tpb}	TPB density (m^{-2})
M	molecular weight ($kg\,mol^{-1}$)
N	molar flux ($mol\,m^{-2}$)
P	pressure or partial pressure (Pa)
p	percolation probability
R_0	universal gas constant ($J\,mol^{-1}\,K^{-1}$)
S	surface area (m^2)
s	molar production or consumption rate ($mol\,m^{-3}\,s^{-1}$)
T	temperature (K)
V_s	volume of solid phase (m^3)
v	volume fraction
w	width (m)
W	width (m)
X	molar fraction

Greek symbols

α	heat-transfer coefficient ($W\,m^{-2}\,K^{-1}$)
ε	porosity
η	overpotential (V)
λ	thermal conductivity ($W\,m^{-1}\,K^{-1}$)
μ	viscosity (Pa s)
σ	conductivity ($S\,m^{-1}$)
τ	tortuosity
ϕ	potential (V)
ϕ_0	Nernst potential (V)
ϕ_{FC}	cell terminal voltage (V)

Subscripts

act	activation
ano	anode
ave	average
bulk	bulk fluid
cath	cathode
ct	charge transfer
con	concentration
el	electronic
ele	electrolyte
h	hydraulic
io	ionic
meso	mesoscale structure
MOLB	mono-block layer built
p	pore
ref	reference
s	solid plate
t	total
tpb	three-phase boundary

Superscripts

eff	effective value
L	per unit length
0	dense material

interface structure such as by using grooves or fins. The electrochemically active area is proportional to the electrode/electrolyte interface area, which is enlarged by the mesoscale control of the interface structure, if the electrochemical reaction takes place close to the electrode/electrolyte interface. Mesoscale-structure control will reduce not only the reaction resistance related to the activation loss but also the electrolyte ohmic resistance.

In this study, we focus on the use of mesoscale-structure control to enlarge the electrode/electrolyte interface area, and we clarify the possibility and effectiveness of using mesoscale-structure control to enhance power generation. A simple theoretical analysis is conducted to find effective conditions such as the electrolyte thickness and operating temperature for mesoscale-structure control. A 2D numerical simulation and a power generation experiment are carried out. We adopt an equivalent electric circuit model and the dusty-gas model for this simulation. We numerically investigate the effect of mesoscale-structure control and discuss the potential and electrochemical reaction distributions in detail, which cannot be measured experimentally. Moreover, we experimentally confirm the effect of mesoscale-structure control by performing the i–V and impedance measurements.

2. Theoretical background

We introduce the theoretical background to mesoscale-structure control by comparing two main resistances of a cell, the ion-conducting resistance and the reaction resistance, to discuss the dominant resistance under a certain range of operating conditions.

SOFCs consist of an electrolyte and two electrodes: an anode and a cathode. The electrolyte only has ohmic resistance to oxide ion conduction. Although the electrodes have three types of resistance, ohmic, reaction (activation), and concentration resistance, the reaction resistance is the main resistance under general operating conditions. Hence, the ionic resistance of the electrolyte and the reaction resistance of the electrodes play important roles in determining the cell performance.

The ratio of electrolyte resistance to reaction resistance is estimated to discuss the dominant resistance for different combinations of temperature and electrolyte thickness. This ratio is defined in Eq. (1), and it is represented by the ratio of the area-specific resistances (ASR) of the electrolyte to that for activation.

$$Bi_{FC} = \frac{1/ASR_{act}}{\sigma_{ele}/l_{ele}} = \frac{1/ASR_{act}}{1/ASR_{ele}} = \frac{ASR_{ele}}{ASR_{act}} \tag{1}$$

This ratio corresponds to a dimensionless number, the Biot number for the heat transfer problem [21], as shown in Table 1. This table shows the analogy between heat transfer and SOFC electrochemistry. Thickness refers to the solid plate thickness in the heat transfer problem and the electrolyte thickness in the SOFC. Thermal conductivity corresponds to the electrolyte ionic conductivity. The heat-transfer coefficient α is the inverse of thermal resistance, i.e., thermal conductance, at the solid/fluid interface, and corresponds to the ASR of the electrochemical reaction at close to the electrode/electrolyte interface. In this paper, the dimensionless number

Table 1
Analogy between heat transfer and SOFC electrochemistry.

	Heat transfer	SOFC
Thickness	l_s [m]	l_{ele} [m]
Conductivity	λ_s [W m^{-1} K^{-1}]	σ_{ele} [S m^{-1}]
Inverse of surface resistance	α [W m^{-2} K^{-1}]	$1/ASR_{act}$ [S m^{-2}]
Dimensionless number	$Bi = \alpha/(\lambda_s/l_s)$	$Bi_{FC} = (1/ASR_{act})/(\sigma_{ele}/l_{ele})$

is referred to as the fuel cell Biot number (FCB), Bi_{FC}. The FCB indicates the dominant resistance that should be reduced to enhance the power generation performance.

Estimated values of ASR including its temperature dependence are used to estimate the variation of FCB under certain operating conditions. The ASR is evaluated in a conventional cell consisting of Ni-yttria-stabilized zirconia cermet (Ni-YSZ) for the anode, YSZ for the electrolyte, and lanthanum strontium manganate (LSM) for the cathode. The ASR of the electrolyte is calculated as the ratio of electrolyte thickness to ionic conductivity, which is estimated as follows [22].

$$\sigma_{YSZ} = \left(0.00294 \ \exp\left(\frac{10350}{T}\right) \times 10^{-2}\right)^{-1} \quad (2)$$

The ASR of activation loss η_{act} is calculated from Eq. (3), and the current densities i (A m^{-2}) are calculated by the Butler-Volmer equations, expressed as Eqs. (4) and (5), for each electrode. $i_{0,ano}$ and $i_{0,cath}$ are the exchange current densities (A m^{-2}) for the anode and cathode, respectively. These standard estimations for the conventional Ni-YSZ/YSZ/LSM cell were proposed by Costamagna and Honegger [23].

$$ASR_{act} = \frac{\eta_{act}}{i} \quad (3)$$

$$i_{ano} = i_{0,ano}\left[\exp\left(\frac{2F}{R_0T}\eta_{act}\right) - \exp\left(\frac{-F}{R_0T}\eta_{act}\right)\right] \quad (4)$$

$$i_{cath} = i_{0,cath}\left[\exp\left(\frac{1.4F}{R_0T}\eta_{act}\right) - \exp\left(\frac{-0.6F}{R_0T}\eta_{act}\right)\right] \quad (5)$$

$$i_{0,ano} = 5.7 \times 10^7 \times \frac{P_{H_2}}{P_{ref}}\left(\frac{P_{H_2O}}{P_{ref}}\right)^{-0.5} \exp\left(\frac{-140000}{R_0T}\right) \quad (6)$$

$$i_{0,cath} = 7 \times 10^9 \times \left(\frac{P_{O_2}}{P_{ref}}\right)^{0.25} \exp\left(\frac{-160000}{R_0T}\right) \quad (7)$$

The FCB is estimated for a temperature range of 600–1000 °C and an electrolyte thickness range of 10–400 μm, with hydrogen, water vapor, and oxygen molar fractions of 0.99, 0.01, and 0.21, respectively.

Fig. 1 shows the variation of FCB for an anode (a) and a cathode (b), where the different lines show different electrolyte thicknesses. The FCB decreases with decreasing electrolyte thickness and increasing operating temperature because of the different tendencies between the ASRs. The FCB is less than unity except when the operating temperature is relatively low and/or the electrolyte thickness is greater than 100 μm. It can be seen that the reaction resistance is the main part of the total resistance of the cell under a wide range of operating conditions. In particular, under a high operating temperature and/or thinner electrolyte (10–20 μm), the FCB is lower than 0.1. A reduction in the electrolyte thickness is

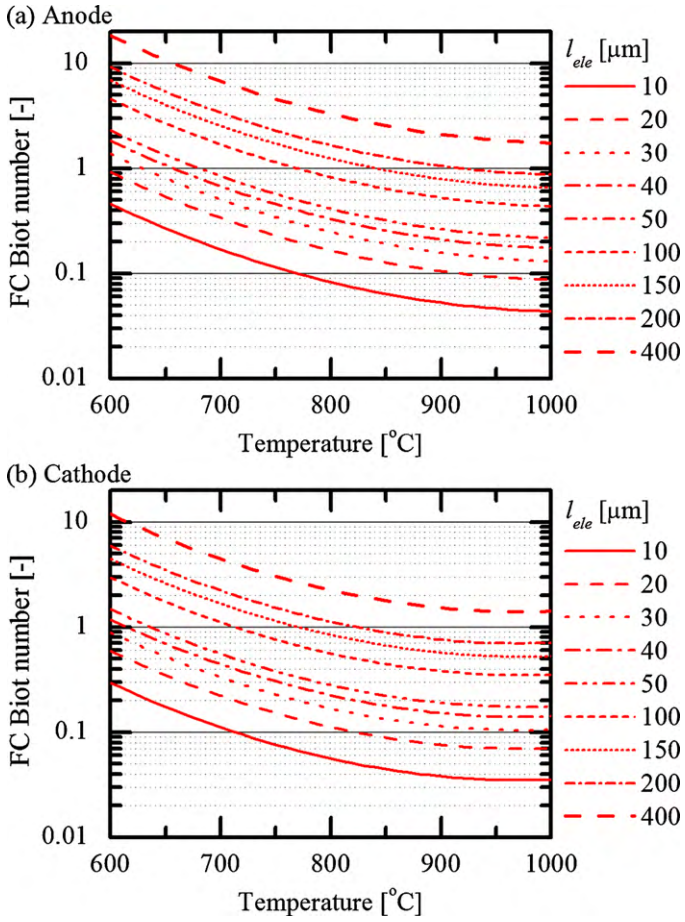

Fig. 1. Temperature and electrolyte thickness dependences of fuel cell Biot number at a current density of 300 mA cm^{-2} for anode (a) and cathode (b).

not effective for enhancing the cell performance under these conditions.

When the reaction resistance is relatively large, namely, $Bi_{FC} < 1$, the enlargement of the interface area by mesoscale-structure control is effective for enhancing the cell performance in a similar way to increasing the heat transfer surface area by fins in heat exchangers.

3. Concept of mesoscale-structure control

Through the discussion based on Bi_{FC}, it is found that the mesoscale-structure control is most effective when the electrolyte is thin, namely, $Bi_{FC} < 1$. Fig. 2(a) shows one possible design of the electrode-supported cell with the corrugated mesoscale structure. Note that this figure shows the anode supported cell but this concept can be applied to the cathode supported cell. For simplicity, we assume that the active TPBs are located in the vicinity of the electrode/electrolyte interfaces and therefore their amount is proportional to the interface area, w. The corrugated structure increases both the anode/and cathode/electrolyte interface area, w, per apparent electrode area, w', and consequently enhances the power density. The enlargement factor can be expressed as $\alpha_{area,meso} = w/w' > 1$. Materials required for this flat cell can be expressed as $l_{ano}w$, $l_{ele}w$, and, $l_{cath}w$ for the anode, electrolyte, and cathode, respectively. By applying the mesoscale structure, we can reduce the anode material as $l_{ano}(w - w')$ and its material cost. The concept to increase the interface area per apparent electrode area can be seen in the mono-block layer built (MOLB) structure [3,7] in macroscopic approach. Fig. 2(b) schematically shows the MOLB concept. The MOLB structure is able to form a flow channel and stack by formation of a corrugated three layers consisted of anode, electrolyte, and cathode. The MOLB cell also increases both electrode/electrolyte interfaces, W, per apparent electrode area, W', by formation of corrugated plate. The enlargement factor can be expressed as $\alpha_{area,MOLB}=W/W' > 1$. The required materials are unchanged and are expressed as $l_{ano}W$, $l_{ele}W$, and $l_{cath}W$ for both the flat and MOLB cell.

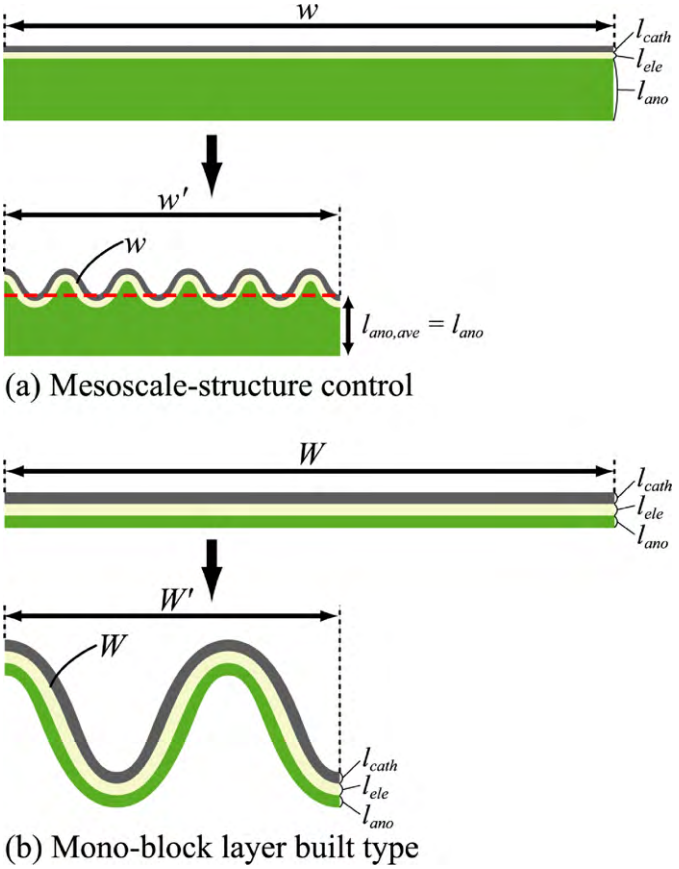

Fig. 2. Concepts of mesoscale structure (a) and MOLB structure (b).

More importantly, it is possible in principle that the approaches with different geometric characteristic length can be applied simultaneously and mutually. Even MOLB cells can be further improved by applying the mesoscale concept. Hence, an approach with new geometric characteristic length is of great importance.

The above discussion is based on the assumption that the electrochemical reactions proceed at the electrode/electrolyte interfaces. In reality, it proceeds not only at the interface but the active TPBs distribute in the porous electrode to a few dozen microns from the interface. It is often referred as an "effective thickness" of electrode [18,19]. Because the characteristic length of the mesoscale structure is close to the effective thickness of electrode, its effectiveness should be carefully discussed. In the following chapters, we perform numerical simulations to consider the local reaction rate in the electrode and the effective thickness.

Before the mesoscale-structure control on thin film electrolyte is tackled, we investigate its effect on simpler condition in this paper. The electrolyte-supported cell and machined mesoscale grooves only on the anode side are adopted due to following reasons. By using the electrolyte-supported cell, we can minimize the effects of the cathode side. The electrolyte-supported cell is easy to produce and use in power generation experiments in laboratory.

4. Methodology

4.1. Simulation method

Fig. 3 shows the computational domains of a standard flat cell and a mesoscale-controlled cell. The mesoscale structure is machined on the anode side of the electrolyte surface to form grooves. The grooves have a rectangular shape and are filled with the anode material as shown in Fig. 3. The electrolyte, anode, and cathode materials are assumed to be YSZ, Ni-YSZ cermet, and LSM-YSZ composite, respectively. We assume isothermal conditions.

In this study, we adopt the electrode microscale model proposed by Nam and Jeon [24] and extend it to perform a 2D simulation. This model calculates the electron and ion transport based on empirical data for the charge transfer current on the TPB by considering the statistical properties of the porous electrodes.

4.1.1. Electron, ion, and mass transport

In this study, we consider the electron, ion, and mass transport in the computational model. The electron and ion transport indicate the conservation of the electronic and ionic currents, respectively. Fig. 4(a) schematically shows the three layers in the computational domain. The gas diffusion layer covers only the two electrodes and is used to calculate the mass transport inside the porous electrodes. The ionic transport layer covers the entire computational domain and is used to calculate the ionic potential. The electron transport layer covers only the two electrodes and is used to calculate the electronic potential. Fig. 4(b) shows the equivalent circuit model in a 1D geometry used to calculate the electronic and ionic potential fields.

The governing equations for the conservation of electronic and ionic currents are expressed as follows.

$$\frac{\partial}{\partial x}\left(\sigma_{el}^{eff}\frac{\partial \phi_{el}}{\partial x}\right) + \frac{\partial}{\partial y}\left(\sigma_{el}^{eff}\frac{\partial \phi_{el}}{\partial y}\right) = -i_{ct} \quad (8)$$

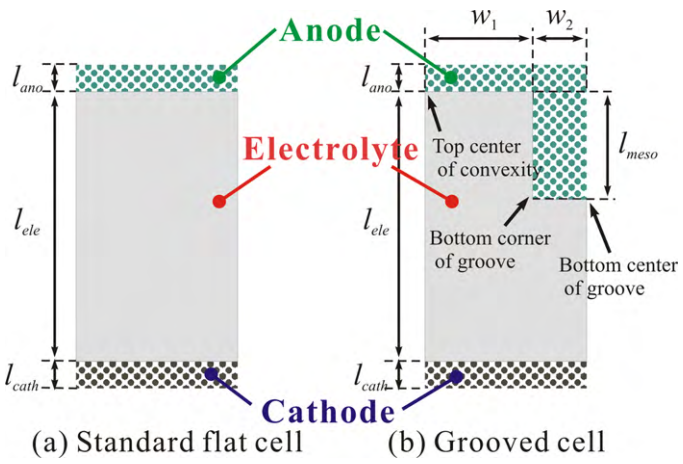

Fig. 3. Simulation models of standard flat cell (a) and cell with mesoscale-structure control (b).

$$\frac{\partial}{\partial x}\left(\sigma_{io}^{eff}\frac{\partial \phi_{io}}{\partial x}\right)+\frac{\partial}{\partial y}\left(\sigma_{io}^{eff}\frac{\partial \phi_{io}}{\partial y}\right)=i_{ct} \tag{9}$$

Note that these equations express the conservation of currents at the anode side. When the conservation equations are used at the cathode side, the right-hand sides of these equations take the opposite sign. i_{ct} represents the volume-specific charge transfer current from the electronic phase to the ionic phase.

The dusty-gas model (DGM) is adopted to simulate the mass transport in the anode and cathode. The DGM can be applied when the Knudsen number is nearly equal to unity and is effective for modeling the mass transport in a multicomponent system in a porous medium such as in SOFC electrodes [25–27]. The DGM is written as Eq. (10) for each chemical component i of the multicomponent system. The permeability K is estimated from the Carman-Konzeny correlation, given by Eq. (11).

$$\frac{N_i}{D_{i,K}^{eff}}+\sum_{j=1,j\neq i}^{n}\frac{X_jN_i-X_iN_j}{D_{ij}^{eff}}=-\frac{P_t}{R_0T}\nabla X_i-\frac{X_i}{R_0T}\left(1+\frac{KP_t}{\mu D_{i,K}^{eff}}\right)\nabla P_t \tag{10}$$

$$K=\frac{\varepsilon^3}{k_K(1-\varepsilon)^2}\left(\frac{V_s}{S}\right)^2=\frac{\varepsilon^3}{k_K(1-\varepsilon)^2}\left(\frac{d_{el}}{6}\right)^2 \tag{11}$$

For a binary system ($n=2$), Eq. (10) can be separated to find the molar flux of each chemical component, and the conservation equations of each chemical component can be rearranged to Eqs. (12)–(18).

$$\frac{\partial}{\partial x}\left(\frac{k_1}{R_0T}\frac{\partial P_1}{\partial x}\right)+\frac{\partial}{\partial y}\left(\frac{k_1}{R_0T}\frac{\partial P_1}{\partial y}\right)+\frac{\partial}{\partial x}\left(\frac{k_2P_1}{R_0T}\frac{\partial P_t}{\partial x}\right)+\frac{\partial}{\partial x}\left(\frac{k_2P_1}{R_0T}\frac{\partial P_t}{\partial y}\right)=s_{ct,1} \tag{12}$$

$$\frac{\partial}{\partial x}\left(\frac{k_3}{R_0T}\frac{\partial P_2}{\partial x}\right)+\frac{\partial}{\partial y}\left(\frac{k_3}{R_0T}\frac{\partial P_2}{\partial y}\right)+\frac{\partial}{\partial x}\left(\frac{k_4P_2}{R_0T}\frac{\partial P_t}{\partial x}\right)+\frac{\partial}{\partial x}\left(\frac{k_4P_2}{R_0T}\frac{\partial P_t}{\partial y}\right)=s_{ct,2} \tag{13}$$

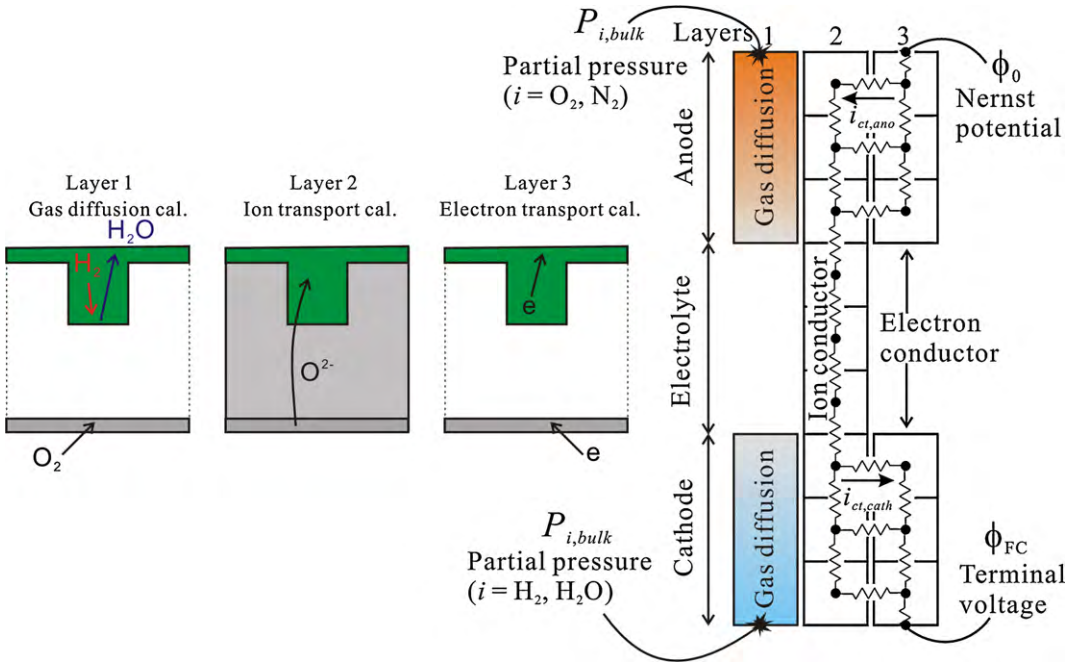

Fig. 4. Three layers used for calculation of gas, oxide ion, and electron transport (left) and equivalent circuit model in one dimension (right).

$$s_{ct,H_2} = \frac{i_{ct}}{2F}, \quad s_{ct,H_2O} = \frac{i_{ct}}{2F} \tag{14}$$

$$s_{ct,O_2} = \frac{i_{ct}}{4F}, \quad s_{ct,N_2} = 0 \tag{15}$$

$$k_1 = \frac{D_{12}^{eff} D_{1,K}^{eff}}{D_{12}^{eff} + D_{m,K}^{eff}}, \quad k_3 = \frac{D_{12}^{eff} D_{2,K}^{eff}}{D_{12}^{eff} + D_{m,K}^{eff}} \tag{16}$$

$$k_2 = k_4 = \frac{1}{P_t} \frac{D_{1,K}^{eff} D_{2,K}^{eff}}{D_{12}^{eff} + D_{m,K}^{eff}} + \frac{K}{\mu} \tag{17}$$

$$D_{m,K}^{eff} = X_1 D_{2,K}^{eff} + X_2 D_{1,K}^{eff} \tag{18}$$

Subscripts 1 and 2 respectively denote H_2 and H_2O on the anode side and O_2 and N_2 on the cathode side. s_{ct} is the molar production or consumption rate of the electrochemical reactions.

The effective diffusivities for binary diffusion and Knudsen diffusion are affected by the properties of the porous electrodes and are expressed as follows.

$$D_{ij}^{eff} = \frac{\varepsilon}{\tau} D_{ij} \quad \text{and} \quad D_{i,K}^{eff} = \frac{\varepsilon}{\tau} D_{i,K} \tag{19}$$

$$D_{i,K} = \frac{d_p}{2} \frac{2}{3} \sqrt{\frac{8R_0T}{\pi M_i}} \tag{20}$$

$$d_p \approx d_h = \frac{4V_s}{S} \frac{\varepsilon}{1-\varepsilon} = \frac{4d_{el}}{6} \frac{\varepsilon}{1-\varepsilon} \tag{21}$$

where D_{ij} and $D_{i,K}$ are the binary and Knudsen diffusivity, respectively, and τ is the tortuosity of the porous electrodes.

4.1.2. Electrochemical reaction model

In the electrochemical reaction model, the oxidation reaction of hydrogen takes place inside the anode and the reduction reaction of oxygen takes place inside the cathode. The volume-specific charge transfer current of these reactions on the TPB is calculated from the volume-specific length of the TPB, evaluated by the random packing model of binary spherical particles and empirical correlations of the charge transfer current per unit TPB length based on the experiments with patterned mesh electrodes. The correlations of the charge transfer current per unit TPB length proposed by Nam and Jeon [24] are derived from the experiments of Bieberle et al. [28] for the anode and from those of Radhakrishnan et al. [29] for the cathode, as shown in Eqs. (22) and (23), respectively. The volume-specific charge transfer current is calculated using Eq. (24).

$$i_{tpb,ano}^{L} = \frac{\eta_{act,ano}}{1.645 P_{H_2}^{-0.11} P_{H_2O}^{-0.67} \exp(10212/T) \times 10^{-4\eta_{act,ano}}} \tag{22}$$

$$i_{tpb,cath}^{L} = \frac{R_0T}{4F} \frac{2 \sinh(2F\eta_{act,cath}/R_0T)}{0.00136 P_{O_2}^{-0.25} \exp(17401/T)} \tag{23}$$

$$i_{ct} = i_{tpb}^{L} l_{tpb} \tag{24}$$

where l_{tpb} is the volume-specific length of the TPB in porous electrodes and is referred to as the TPB density.

The activation overpotential in this model is calculated as the potential difference between the electronic and ionic phases in the electrode at each grid, as shown in Eqs. (25) and (26). This value is used to calculate the charge transfer current.

$$\eta_{act,ano} = \phi_{el} - \phi_{io} - \eta_{con,ano} \tag{25}$$

$$\eta_{act,cath} = \phi_{io} - \phi_{el} - \eta_{con,cath} \tag{26}$$

Table 2
Calculation conditions.

Calculation parameter	Anode	Cathode
Operating temperature T	800 °C	800 °C
Total pressure P_t	0.1013 MPa	0.1013 MPa
Gas compositions	$X_{H_2} : X_{H_2O}$ = 0.99 : 0.01	$X_{O_2} : X_{N_2}$ = 0.21 : 0.79
Tortuosity τ	3.0	3.0
Porosity ε	0.3	0.3
Volume fraction of electron v_{el}	0.35	0.35
Volume fraction of ion v_{io}	0.35	0.35
Particle size of electron d_{el}	1 μm	1 μm
Particle size of ion d_{io}	1 μm	1 μm
Percolation prob. of electron p_{el}	0.925	0.925
Percolation prob. of ion p_{io}	0.925	0.925
TPB density l_{tpb}	1.40 μm^{-2}	1.40 μm^{-2}
Electrode thickness l_i	50 μm	50 μm
Kozeny constant k_K	5	5

The concentration overpotential is calculated as the effect of the partial pressure change on the Nernst potential and is included in the calculations of the activation overpotential.

$$\eta_{con,ano} = \frac{R_0T}{2F} \ln\left(\frac{P_{H_2,bulk}}{P_{H_2}} \frac{P_{H_2O}}{P_{H_2O,bulk}}\right) \tag{27}$$

$$\eta_{con,cath} = \frac{R_0T}{4F} \ln\left(\frac{P_{O_2,bulk}}{P_{O_2}}\right) \tag{28}$$

The effective conductivity is adopted for the porous electrode properties, where we consider the statistical percolation probability. The effective conductivity of an electrode is expressed as follows.

$$\sigma_i^{eff} = (v_i p_i)^{1.5} \sigma_i^0 \tag{29}$$

In this equation, subscript i denotes an electronic transport phase (el) composed of an electron-conducting material, or an ionic transport phase (io) composed of an ion-conducting material. σ_i^0 is the conductivity (S cm^{-1}) of the dense material i. v_i is the volume fraction of phase i ($v_{el} + v_{io} + \varepsilon = 1$). p_i is the percolation probability. The conductivities of the dense materials are given by Eqs. (30)–(32), and are obtained from the literature [22,24,30,31].

$$\sigma_{YSZ}^0 = \left(0.00294 \exp\left(\frac{10350}{T}\right)\right)^{-1} \tag{30}$$

$$\sigma_{Ni}^0 = \frac{4.5 \times 10^5}{T} \exp\left(-\frac{1200}{T}\right) \tag{31}$$

$$\sigma_{LSM}^0 = 3.27 \times 10^4 - 10.653T \tag{32}$$

4.1.3. Calculation conditions

Table 2 shows the calculation conditions such as the operating temperature, along with the parameters and properties of the porous electrodes in this simulation. d_{el} and d_{io} are the particle diameters in the electron- and ion-conducting phases, respectively. These values are used to calculate the percolation probability and the TPB density by the random packing model. In the boundary conditions for the gas diffusion layer on the horizontal surface, the partial pressure is given by that of the bulk gas phase from the gas composition at atmospheric pressure. The boundary condition of the electron transport layer is given as the potential difference between the electrode surfaces. In this model, we assume that the electronic potentials of the boundary are given as the Nernst potential, which is calculated using Eq. (33) for the anode surface and using the cell terminal voltage for the cathode surface. We assume that the vertical boundaries of the three layers have symmetric

boundary conditions expressed as zero gradients.

$$\phi_0 = E_0 + \frac{RT}{2F} \ln\left(\frac{P_{H_2,bulk}}{P_{H_2O,bulk}}\left(\frac{P_{O_2,bulk}}{10130}\right)^{0.5}\right) \quad (33)$$

We focus on the two mesoscale parameters of the anode/electrolyte interface area and the mean electrolyte thickness in this study, because the anode mesoscale structure affects both the anode/electrolyte interface area and the electrolyte thickness. Table 3 shows three cases with different values for the mesoscale parameters of the grooved cell. Case SG shows small mesoscale grooves compared with others. Cases 1–3 have the same mean electrolyte thickness but different area enlargement factors, expressed as follows.

$$\text{Area enlargement factor} = \frac{\text{Interface area with grooves}}{\text{Interface area without grooves}} = \frac{w_1 + w_2 + l_{meso}}{w_1 + w_2} \quad (34)$$

The average current density is the total current at the cathode surface boundary divided by the electrode/electrolyte interface area of the flat side, which is expressed as follows.

$$i_{ave} = \frac{\sum_x I_{y=0}}{w_1 + w_2} \quad (35)$$

Note that in this equation, $y = 0$ mm corresponds to the cathode surface.

4.2. Experimental method

In this section, we explain the experimental method used in the power generation test, which involves a segmented electrode with both flat and mesoscale-grooved surface in a button-type cell. The segmented electrode is used to remove the issue of the reproducibility of the cells as much as possible, as it makes it allow the easy comparison of a flat cell with a mesoscale-grooved cell. The power generation performance of each cell is evaluated in terms of the *i*–*V* characteristics and impedance spectra.

Fig. 5 shows a schematic diagram of the experimental apparatus used in this study. A button-type cell is sandwiched between two sets of coaxial ceramic tubes. On the lower side of the anode, fuel is supplied through the inner tube to the cell. It impinges on the cell and then returns through the gap between the inner tube and outer tube to be exhausted. The fuel is a mixture of hydrogen and nitrogen. The hydrogen concentration in the fuel flow is precisely controlled using mass flow controllers. The situation is exactly the same on the upper side of the cathode, but the fluid is dry air. Both outer tubes are tightly connected to the cell by a glass seal to prevent gas leakage. In the experiments, the hydrogen concentration of the fuel is varied at a constant operating temperature of 800 °C.

In an actual SOFC system, this high operating temperature is self-sustained by heat generated by the electrochemical reactions. However, in a single-cell experiment some additional heat must be supplied to maintain the operating temperature. Therefore, the entire test section is placed in an electric furnace in this study.

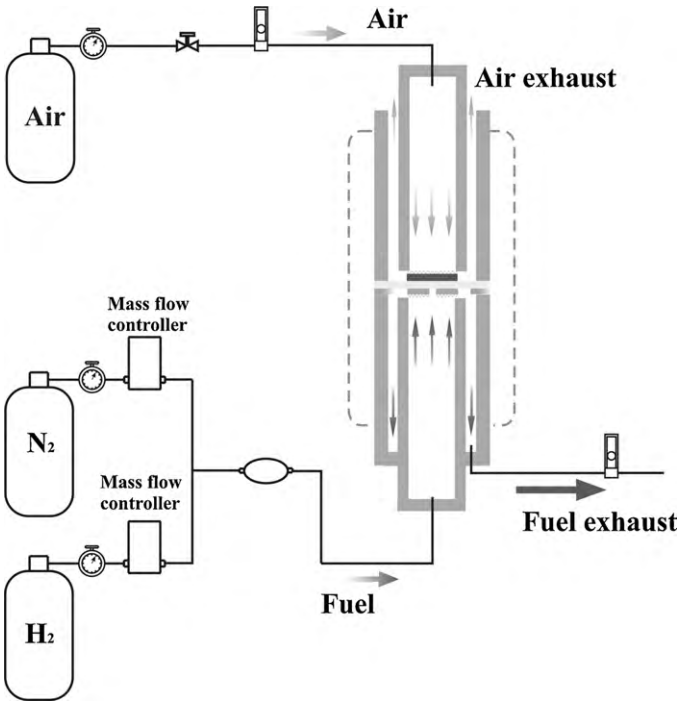

Fig. 5. Experimental apparatus used for power generation test involving button-type cell.

Fig. 6(a) shows the electrolyte of the test cell, which is a small disk-shaped electrolyte made of YSZ with a diameter and thickness of 20 mm and 500 μm, respectively. A surface on the anode side shown in Fig. 6(a) is partially machined to realize mesoscale-grooved structures by using the blasting method. The groove width is 200 μm at the surface and the distance between two neighboring grooves is 250 μm. The groove shape is not exactly same as the well-defined shape in simulation because precise fabrication of rectangular grooves was difficult. Fortunately, uniformity of the groove shape was quite good and therefore we can precisely measure the surface area. The electrolyte surface is flat on the cathode side.

Electrode materials are prepared by following the procedure [32]. The cathode material, LSM, is mixed with polyethylene glycol to form a slurry, which is screen-printed on the electrolyte and sintered at 1150 °C for 5 h. The anode material, NiO-YSZ, is also mixed with polyethylene glycol, screen-printed on the electrolyte, and sintered at 1400 °C for 5 h. As can be observed in Fig. 6(b), the anode electrode is segmented into two parts. The left side of Fig. 6(b) shows the flat surface of the electrolyte and the right side shows the grooved surface. Power generation tests using each anode electrode are conducted separately and the results are compared. The reason for using such segmented electrodes rather than preparing two cells (one with a standard flat electrode and the other with a mesoscale structure) is to avoid the issue of the reproducibility of the cells.

Fig. 7 is an SEM image showing cross-sectional view of grooved part of a test cell. This image confirms that each groove is 200 μm

Table 3
Mesoscale parameters of grooved cell.

	w_1 [μm]	w_2 [μm]	l_{meso} [μm]	l_{ele} [μm]	Mean electrolyte thickness [μm]	Area enlargement factor
Flat cell				433	433	1.00
Case SG	10	5	10	438	433	1.67
Case 1	300	150	200	500	433	1.44
Case 2	200	100	200	500	433	1.67
Case 3	100	50	200	500	433	2.33

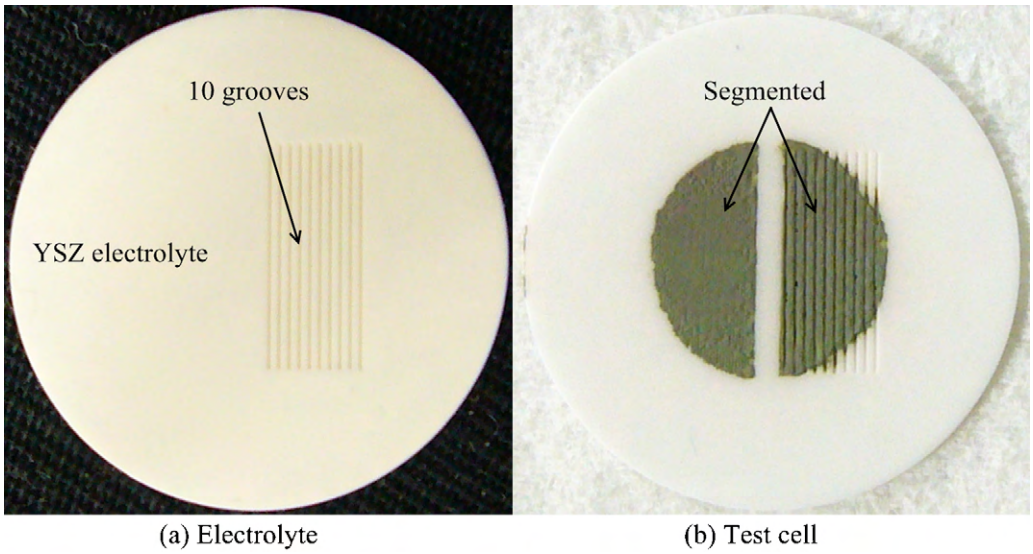

Fig. 6. Anode-side surface of an electrolyte (a) and a test cell coated with segmented anode (b).

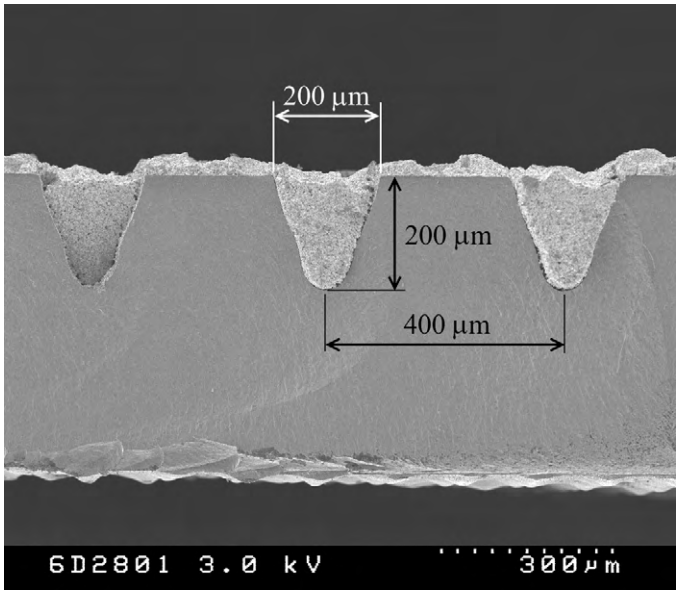

Fig. 7. SEM image of part of the grooved area of a cell filled with the Ni-YSZ anode material.

deep and filled with the anode material. It also confirms that the shape of the grooves is well controlled. The enlargement of the interface area between the electrolyte and anode electrode is estimated to be 60% compared with that for a flat interface. This grooved structure is different to that of the calculation model as indicated above (Section 4.1).

To collect the current from the electrodes, a thin platinum mesh is attached to each electrode. As the anode electrode is segmented into two parts, two sets of current collectors are carefully placed on each anode electrode so that there is no electrical contact between the two anode electrodes. A platinum wire with a diameter of 0.5 mm is connected to each platinum mesh and the current is conducted to outside the test section. For voltage measurement, a thinner platinum wire with a diameter of 0.2 mm is also connected to each platinum mesh. One additional platinum wire is directly connected to the outer part of the electrolyte as a reference electrode. An impedance meter (Kikusui KFM2150) with an electronic load (Kikusui PLZ164WA) is connected to the test cell, as shown in Fig. 8, to obtain the *i–V* curve and perform impedance measurements.

5. Results and discussion

5.1. Simulation results

5.1.1. Effect of small anode mesoscale structure

Fig. 9 shows the anode volume-specific charge transfer current distributions at the terminal voltage of 0.5 V in Case SG. This case has the groove height of 10 μm. It is found from this figure that the mesoscale structure is covered with the reaction region when the scale of this structure becomes too small compared with that of the reaction region. The values of average current density of this case and the flat case with the same mean electrolyte thickness are 265 and 259 mA cm^{-2}, respectively. Such structure is not useful to enhance the cell performance. It should be designed that the mesoscale structure becomes larger than the effective thickness of electrode.

5.1.2. Effect of anode mesoscale structure on i–V characteristics

Fig. 10 shows the *i–V* characteristics of the cells with grooves (Cases 1–3), along with that of a standard flat cell with an electrolyte thickness of 433 μm.

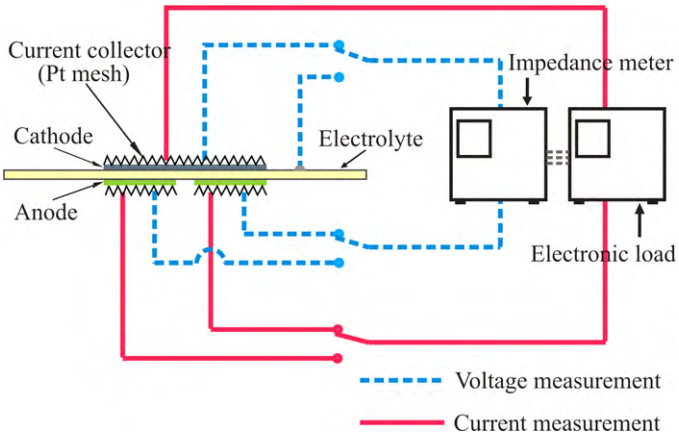

Fig. 8. Measurement system used for segmented anode using four-probe method.

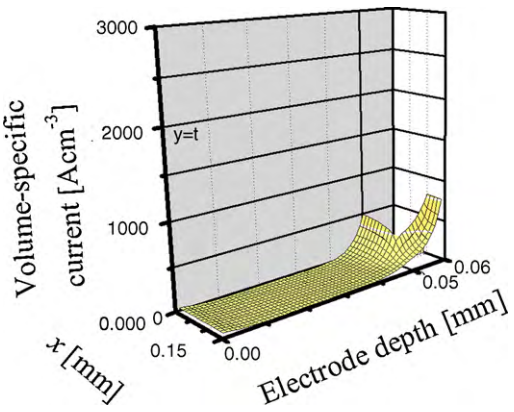

Fig. 9. Volume-specific charge transfer current distribution of anode in Case SG.

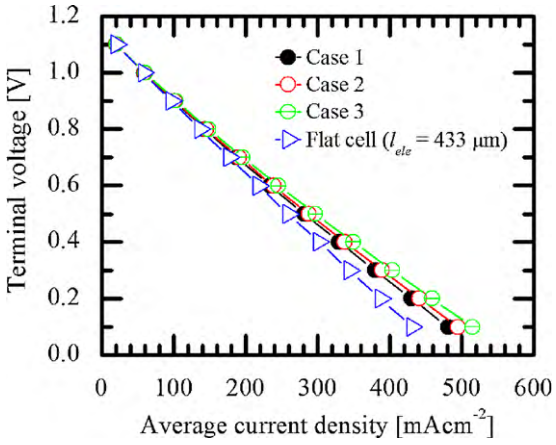

Fig. 10. *i–V* characteristics of flat cell and grooved cells (Cases 1–3).

The *i–V* curves of the mesoscale-grooved cells show a similar trend to that of the flat cell in Fig. 10. The terminal voltage decreases almost linearly with increasing current density. The current densities of the grooved cells are almost always larger than that of the flat cell at the same terminal voltage. This confirms that the mesoscale-grooved structure enhances the power generation performance.

Fig. 11 shows the average current density enhancement, defined as the ratio of the current density of a grooved cell to that of a flat cell having the same electrolyte thickness at the same terminal voltage.

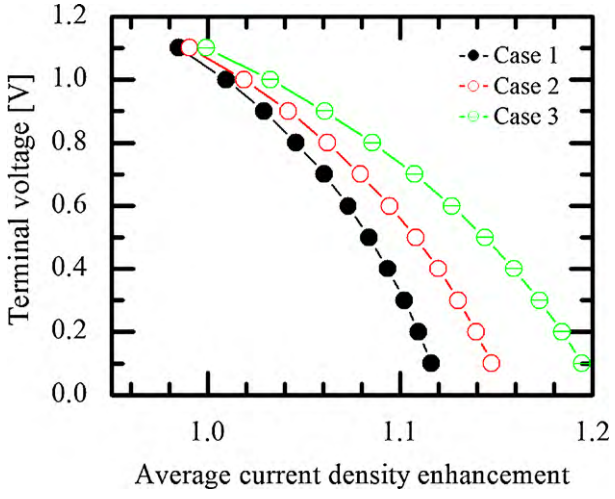

Fig. 11. Average current density enhancement by mesoscale grooves for Cases 1–3.

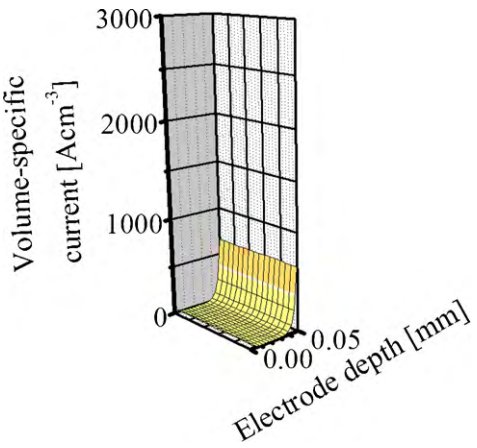

Fig. 12. Volume-specific charge transfer current distribution of the flat anode at a terminal voltage of 0.5 V.

This value represents the enhancement of cell performance due to the mesoscale grooves.

$$\text{Average current density enhancement} = \frac{\text{Current density with grooves}}{\text{Current density without grooves}} \quad (36)$$

It is shown in Figs. 10 and 11 that the larger interface area of the grooved cell results in a better cell performance. The average current density enhancement becomes more prominent when the current density is relatively high. The current density enhancement values of Cases 1, 2, and 3 at the terminal voltage of 0.5 V are about 1.08, 1.11, and 1.14, respectively. Because all of the cases in Fig. 11 have the same mean electrolyte thickness, the effect of the mesoscale grooves on the cell performance cannot be ascribed to the mean electrolyte thickness. These enhancement values are less than the area enlargement factor. This is reasonable if we consider the reaction region spread in the electrode as discussed in the previous section. Other reasons can be the thick electrolyte and mal-distribution of current.

5.1.3. Electrochemical reaction and potential distributions

In this section, we explain in detail the effects of the anode mesoscale grooves from the simulation results for Case 2 at a terminal voltage of 0.5 V. The volume-specific charge transfer current distributions are illustrated in Fig. 12 for the flat anode and in Fig. 13

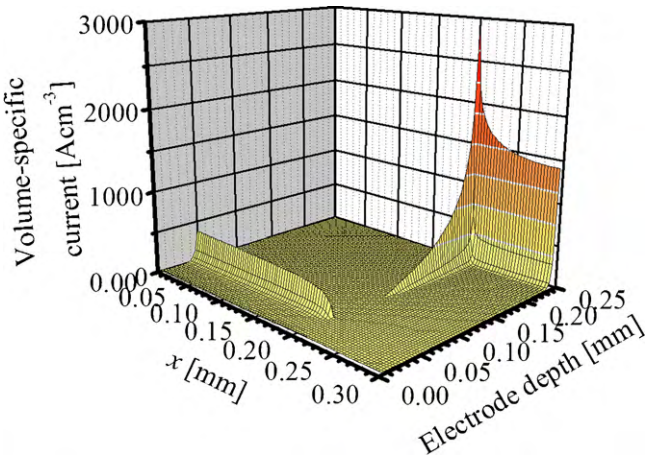

Fig. 13. Volume-specific charge transfer current distribution of anode in Case 2 at a terminal voltage of 0.5 V.

Table 4
Anode and cathode overpotentials and partial pressures at the top center of convexity, bottom corner of groove, bottom center of groove, and cathode bottom at a terminal voltage of 0.5 V in Case 2.

	Location	Depth [μm]	η_{act} [mV]	η_{con} [mV]	P_{H_2} [kPa]	P_{H_2O} [kPa]
Anode	Top center of convexity	50	12	14	1000	1.36
	Bottom corner of groove	250	27	94	952	7.39
	Bottom center of groove	250	15	89	950	6.58
Cathode	Bottom (max)	50	107	0.45		

for the grooved anode. The volume-specific current corresponds to the local electrochemical reaction rate. Note that in Fig. 12, the electrode depths of 0 and 0.05 mm correspond to the anode surface and the flat anode/electrolyte interface, respectively. In Fig. 13, the electrode depths of 0, 0.05, and 0.25 mm correspond to the anode surface, the top of a convexity, and groove bottom, respectively.

It can be seen in Fig. 12 that the volume-specific current in the flat anode takes a larger value near the anode/electrolyte interface and is distributed uniformly in the x-direction. In the grooved anode, as shown in Fig. 13, the volume-specific current is not uniform and is large inside the grooved part, particularly at the bottom corner of groove. This shows that the electrochemical reaction is active at such regions. This region is surrounded by the electrolyte with relatively high ion potential. It leads the ion potential at the bottom corner becomes higher than that of other reaction region. Hence the active electrochemical reaction at such region is reasonable. The sharp edge in the calculation domain may lead an overestimation of the reaction at the bottom corner point.

This difference in the reaction region is caused by the different electric potentials and different partial pressures of the chemical species. We calculated the electronic and ionic potentials and obtained their distributions in this simulation. The electronic potential field of the electrodes is found to be uniform owing to the low ohmic resistance to electronic conduction of the electrodes. The oxide ion potential fields for Cases 1–3 are illustrated in Fig. 14. In this figure, the dotted lines show the electrode/electrolyte interfaces. Note that $y = 0$ mm and $y = 0.6$ mm correspond to the cathode and anode surfaces, respectively. Table 4 shows the local values of the activation and concentration overpotentials and the partial pressure at some important locations, namely, the top centers of a convexity, the bottom corner of groove, and the bottom center of a groove for the anode, as shown in Fig. 3(b), and the cathode/electrolyte interface for the cathode. From Fig. 14 and Table 4, the large potential difference in the electrolyte shows that the electrolyte resistance is a main resistance due to the thick electrolyte. It can be seen that the potential difference between the anode/electrolyte interfaces at the top of a convexity and the groove bottom is about 0.08 V. Such a potential difference is comparable to the difference between the concentration overpotentials at each location, as shown in Table 4, due to the depth of 250 μm. Hence the activation overpotential of the top of a convexity is comparable to that of the groove bottom. However, the volume-specific current at the groove bottom is at least threefold higher than that at the top of a convexity, because the groove bottom has a relatively high vapor partial pressure, which is affected by the charge transfer current given by Eq. (22).

Fig. 15 shows the proportion of the charge transfer current occurring at the top of a convexity, the side wall of the grooves, and the groove bottom in the three cases. The percentages are calculated from the total charge transfer current up to 10 μm from the electrode/electrolyte interface at the different locations. Note that a value of 100% on the vertical axis represents the total charge transfer current for the flat anode. The percentage of the charge transfer current in the neighborhood of the side wall increases with the area enlargement factor. Hence, this figure indicates that the total charge transfer current increases with the area enlargement factor due to the contribution of the side wall. In these cases, the area enlargement factor is directly related to the proportion of the area corresponding to the side wall, and increases the pro-

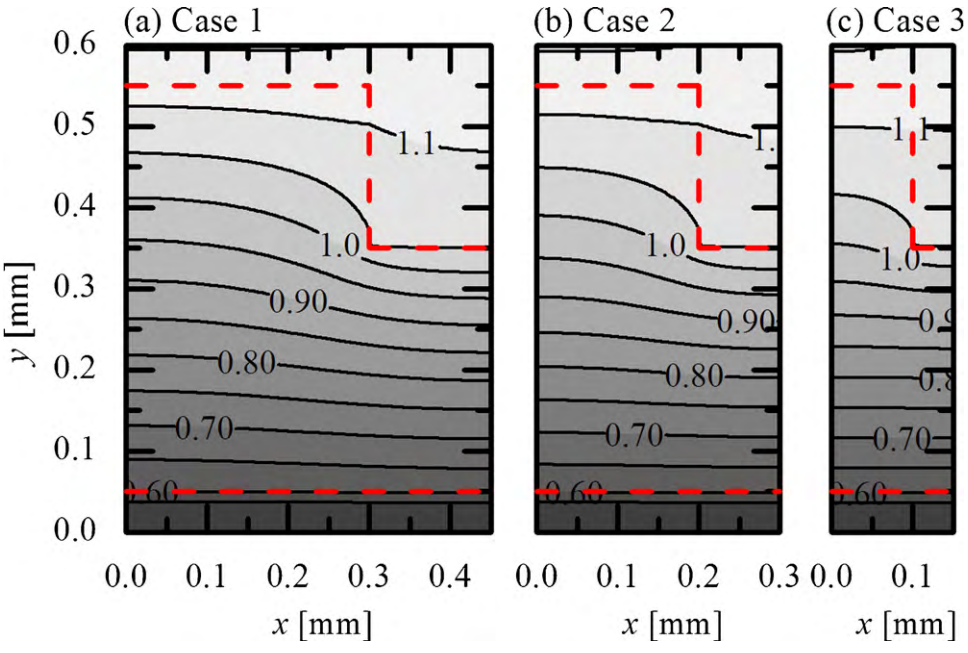

Fig. 14. Oxide ion potential fields of Case 1 (a), Case 2 (b), and Case 3 (c) at a terminal voltage of 0.5 V.

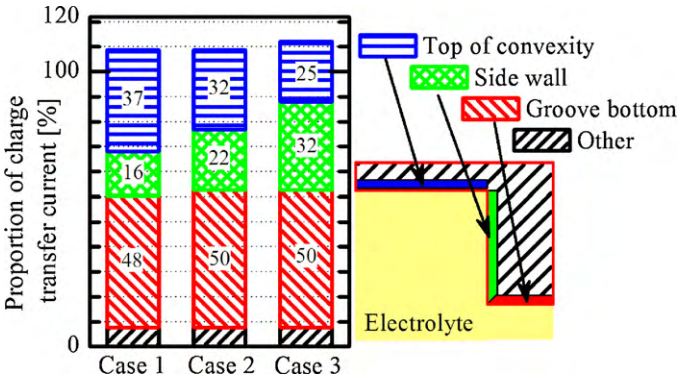

Fig. 15. Proportion of charge transfer reaction occurring at the top of a convexity, side wall, and groove bottom in the anode electrode. 100% on the vertical axis indicates the charge transfer current for the flat anode.

portion of the active region because the groove bottom is at a relatively high vapor partial pressure. An increase in the proportion of such an active region yields an increase in the average current density.

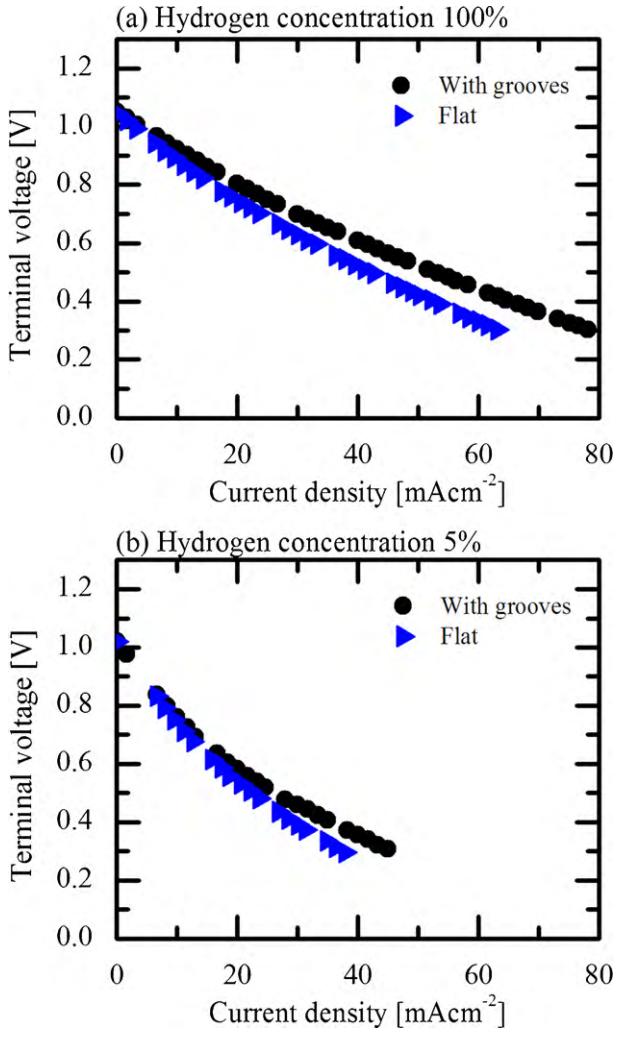

Fig. 16. Comparison of *i–V* characteristics of segmented electrodes for cell at operating temperature of 800 °C with hydrogen concentration of 100% (a) and 5% (b).

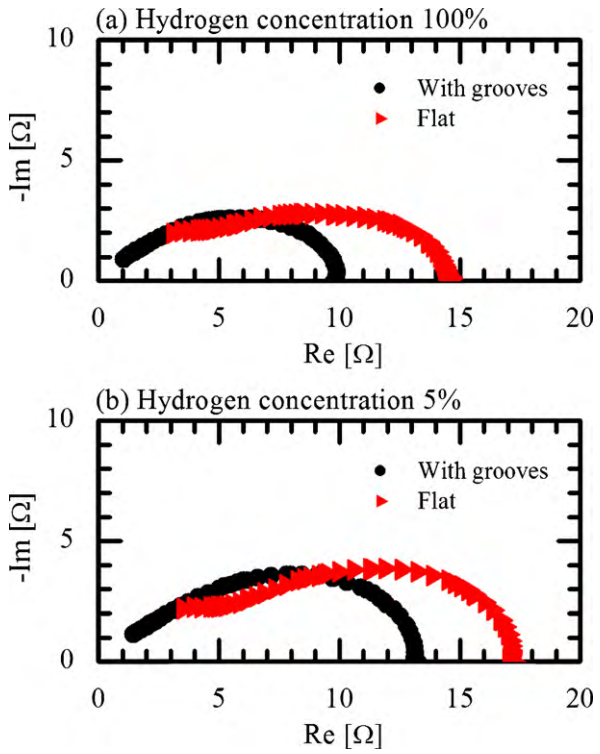

Fig. 17. Impedance spectra measured between anode and electrolyte at operating temperature of 800 °C with hydrogen concentration of 100% (a) and 5% (b).

5.2. Experimental results

In this section, we discuss the effect of the mesoscale-structure control on the power generation performance observed in the experiment. Fig. 16 shows the *i–V* curves of the flat and mesoscale-grooved cells. In this figure, the solid triangles and solid circles denote the results for the flat cell and grooved cell, respectively. Note that the flat cell has a different mean electrolyte thickness from the grooved cell. The performance of the grooved cell is higher than that of the flat cell at all terminal voltages. It can be seen that the grooves enhance the cell performance owing to the reduction of the electrolyte thickness and the enlargement of the interface area. The current density of the grooved cell is 25% and 16% higher than that of the flat cell at hydrogen concentrations of 100% and 5%, respectively, at a terminal voltage of 0.5 V.

The experimental current density enhancement does not quantitatively agree with that of simulation. A main reason is the estimation of electrode microstructure by using the model based on the random packing model. It is difficult to reconstruct the microstructural parameters of the experimental cell. However, the qualitative agreement of the area enlargement effect between the simulation and experiment is confirmed.

We can clarify the effect of enlarging the electrode/electrolyte interface by considering the impedance spectra measured between the anode and the reference electrode attached to the electrolyte, because the *i–V* curve includes not only the effect of interface enlargement but also that of decreasing the electrolyte thickness. Fig. 17 shows a comparison of the impedance spectra of the flat and mesoscale-grooved cells. Impedance arcs related to the anodic electrochemical reaction are observed. Owing to the frequency limit of the measurement system, the left end of each arc is not clear. Because of the grooves, the mean electrolyte thickness is lower for the anode grooves, giving one reason for its better performance. The difference between the ohmic resistances of the two cells is evaluated to be 1.2 Ω using the mean electrolyte thickness. However,

from Fig. 17, the difference between the right ends of each arc is about 4.9 Ω (4 Ω at a hydrogen concentration of 5%), which is larger than 1.2 Ω. This means that the thinner electrolyte is not the only reason for the better performance. The concentration overpotential in the anode with grooves is expected to be larger than that for the flat anode. The enhancement of the power generation performance is a result of the apparent decrease in the activation overpotential caused by the enlargement of the active area due to the grooves.

6. Conclusion

In this paper, we numerically and experimentally investigated the effect of mesoscale-structure control on enhancing the power generation performance.

A simple theoretical analysis was conducted in the light of the dimensionless number, FCB. It was assumed that the electrochemical reaction takes place only on the electrode/electrolyte interface. From the simple analysis, the FCB was found to be lower than unity when a relatively thin electrolyte (10–20 μm) was employed and/or the operating temperature is increased in a conventional Ni-YSZ/YSZ/LSM cell. Under these conditions, the power generation performance can be effectively enhanced by reducing the reaction resistance. The corrugated mesoscale structure in the electrode-supported cell was proposed to reduce the reaction resistance for the practical application.

Because the electrochemical reaction in electrode actually has an effective thickness, we performed numerical simulations and power generation experiments to clarify the effectiveness of mesoscale structure. Thick electrolyte was used to focus on one side of the electrolyte, i.e., the anode side, while eliminating the effects of the other side. The microstructural parameters of electrode were estimated on the basis of the random packing model in numerical simulations. The segmented electrode was used in experiments to realize the precise comparison between the flat cell and the mesoscale-grooved cell. We reported the following results.

(1) We found from the simulation results that the electrochemical reaction is limited to the region close to the electrode/electrolyte interface. The mesoscale-grooved structure was proved to be effective for enhancing the power generation performance, if the groove scale is sufficiently larger than the effective thickness of the electrode.
(2) The qualitative agreement of the area enlargement effect between the simulation and experiment is confirmed. The improvement of the accuracy in the microstructural parameter estimation is required to obtain more quantitative agreement.
(3) From the simulation results of the mesoscale-grooved cell, the electrochemical reaction actively takes place at the groove bottom, because of the similar activation overpotentials and the higher vapor partial pressure compared with those at the top of a convexity.
(4) The expected impedance arc of the grooved cell was smaller than that of the flat cell from the impedance measurement. This confirms that the mesoscale-grooved structure can reduce the reaction resistance.

Acknowledgements

This study is partially supported by the European Commission (project Dev-BIOSOFC, FP6-042436, MTKD-CT-2006-042436). The authors at Kyoto University are supported by the New Energy and Industrial Technology Development Organization (NEDO) under the Development of System and Elemental Technology on Solid Oxide Fuel Cell (SOFC) Project.

References

[1] T. Ishihara, H. Matsuda, Y. Takita, J. Am. Chem. Soc. 116 (1994) 3801–3803.
[2] K.C. Wincewicz, J.C. Cooper, J. Power Sources 140 (2005) 280–296.
[3] S.A. Barnett, Energy 15 (1) (1990) 1–9.
[4] S.C. Singhal, Solid State Ionics 135 (2000) 305–313.
[5] N.M. Sammes, Y. Du, R. Bove, J. Power Sources 145 (2005) 428–434.
[6] T. Suzuki, T. Yamaguchi, Y. Fujishiro, M. Awano, J. Power Sources 160 (2006) 73–77.
[7] J.J. Hwang, C.K. Chen, D.Y. Lai, J. Power Sources 140 (2005) 235–242.
[8] J.-H. Kim, R.-H. Song, K.-S. Song, S.-H. Hyun, D.-R. Shin, H. Yokokawa, J. Power Sources 122 (2003) 138–143.
[9] Y. Lu, L. Schaefer, P. Li, J. Power Sources 140 (2005) 331–339.
[10] Y.C. Hsiao, J.R. Selman, Solid State Ionics 98 (1997) 33–38.
[11] D. Simwonis, F. Tietz, D. Stover, Solid State Ionics 132 (2000) 241–251.
[12] M.J. Jørgensen, P. Holtappels, C.C. Appel, J. Appl. Electrochem. 30 (2000) 411–418.
[13] Y.L. Liu, S. Primdahl, M. Mogensen, Solid State Ionics 161 (2003) 1–10.
[14] H. Yokokawa, H. Tu, B. Iwanschitz, A. Mai, J. Power Sources 182 (2008) 400–412.
[15] T. Kenjo, M. Nishiya, Solid State Ionics 57 (1992) 295–302.
[16] E.P. Murray, T. Tsai, S.A. Barnett, Solid State Ionics 110 (1998) 235–243.
[17] V.A.C. Haanappel, J. Mertens, D. Rutenbeck, C. Tropartz, W. Herzhof, D. Sebold, F. Tietz, J. Power Sources 141 (2005) 216–226.
[18] T. Kenjo, S. Osawa, K. Fujikawa, J. Electrochem. Soc. 138 (2) (1991) 349–355.
[19] S. Sakamoto, H. Taira, H. Takagi, Denki Kagaku 64 (6) (1996) 609–613.
[20] J. Will, A. Mitterdorfer, C. Kleinlogel, D. Perednis, L.J. Gauckler, Solid State Ionics 131 (2000) 79–96.
[21] J.P. Holman, Heat Transfer, 8th ed., McGraw-Hill, 1997.
[22] N.F. Bessette II, W.J. Wepfer, J. Winnick, J. Electrochem. Soc. 142 (11) (1995) 3792–3800.
[23] P. Costamagna, K. Honegger, J. Electrochem. Soc. 145 (11) (1998) 3995–4007.
[24] J.H. Nam, D.H. Jeon, Electrochim. Acta 51 (2006) 3446–3460.
[25] E.A. Mason, A.P. Malinauskas, R.B. Evans III, J. Chem. Phys. 46 (8) (1967) 3199–3216.
[26] D. Arnost, P. Schneider, Chem. Eng. J. 51 (1995) 91–99.
[27] R. Suwanwarangkul, E. Croiset, M.W. Fowler, P.L. Douglas, E. Entchev, M.A. Douglas, J. Power Sources 122 (2003) 9–18.
[28] A. Bieberle, L.P. Meier, L.J. Gauckler, J. Electrochem. Soc. 148 (6) (2001) 646–656.
[29] R. Radhakrishnan, A.V. Virkar, S.C. Singhal, J. Electrochem. Soc. 152 (1) (2005) 210–218.
[30] U. Anselmi-Tamburini, G. Chiodelli, M. Arimondi, F. Maglia, G. Spinolo, Z.A. Munir, Solid State Ionics 110 (1998) 35–43.
[31] J.R. Ferguson, J.M. Fiard, R. Herbin, J. Power Sources 58 (1996) 109–122.
[32] T. Takeguchi, Y. Kani, T. Yano, R. Kikuchi, K. Eguchi, K. Tsujimoto, Y. Uchida, A. Ueno, K. Omoshiki, M. Aizawa, J. Power Sources 112 (2002) 588–595.